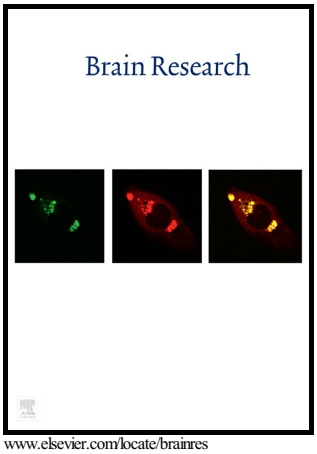

www.elsevier.com/locate/brainres

Spatial patterns and cell surface clusters in perineuronal nets

Nikita Arnst, Svetlana Kuznetsova, Nikita Lipachev, Nurislam Shaikhutdinov, Anastasiya Melnikova, Mikhail Mavlikeev, Pavel Uvarov, Tatyana V. Baltina, Heikki Rauvala, Yuriy N. Osin, Andrey P. Kiyasov, Mikhail Paveliev

PII: S0006-8993(16)30493-0
DOI: http://dx.doi.org/10.1016/j.brainres.2016.07.020
Reference: BRES45019

To appear in: *Brain Research*

Received date: 15 December 2015
Revised date: 29 June 2016
Accepted date: 13 July 2016

Cite this article as: Nikita Arnst, Svetlana Kuznetsova, Nikita Lipachev Nurislam Shaikhutdinov, Anastasiya Melnikova, Mikhail Mavlikeev, Pave Uvarov, Tatyana V. Baltina, Heikki Rauvala, Yuriy N. Osin, Andrey P. Kiyasov and Mikhail Paveliev, Spatial patterns and cell surface clusters in perineurona nets, *Brain Research,* http://dx.doi.org/10.1016/j.brainres.2016.07.020

Spatial patterns and cell surface clusters in perineuronal nets

Nikita Arnst[a,b], Svetlana Kuznetsova[c], Nikita Lipachev[a], Nurislam Shaikhutdinov[b], Anastasiya Melnikova[b], Mikhail Mavlikeev[b], Pavel Uvarov[a], Tatyana V. Baltina[b], Heikki Rauvala[a], Yuriy N. Osin[c], Andrey P. Kiyasov[b], Mikhail Paveliev[a,b,*]

[a]Neuroscience Center, University of Helsinki, Viikinkaari 4 00790 P.O.Box 56 Helsinki, Finland
[b]Institute of Fundamental Medicine and Biology, Kazan Federal University Kazan K.Marx 74 420012 Tatarstan Russia

[c]Interdisciplinary Center for Analytic Microscopy, Kazan Federal University Kazan Parizhskoy Kommuny Str 9 420021 Tatarstan Russia

[*]Corresponding author Mikhail Paveliev. paveliev@helsinki.fi

Abstract

Perineuronal nets (PNN) ensheath GABAergic and glutamatergic synapses on neuronal cell surface in the central nervous system (CNS), have neuroprotective effect in animal models of Alzheimer disease and regulate synaptic plasticity during development and regeneration. Crucial insights were obtained recently concerning molecular composition and physiological importance of PNN but the microstructure of the network remains largely unstudied. Here we used histochemistry, fluorescent microscopy and quantitative image analysis to study the PNN structure in adult mouse and rat neurons from layers IV and VI of the somatosensory cortex. Vast majority of meshes have quadrangle, pentagon or hexagon shape with mean mesh area of 1.29 μm^2 in mouse and 1.44 μm^2 in rat neurons. We demonstrate two distinct patterns of chondroitin sulfate distribution within a single mesh – with uniform (nonpolar) and node-enriched (polar) distribution of the *Wisteria floribunda* agglutinin-positive signal. Vertices of the node-enriched pattern match better with local maxima of chondroitin sulfate density as compared to the uniform pattern. PNN is organized into clusters of meshes with distinct morphologies on the neuronal cell surface. Our findings suggest the role for the PNN microstructure in the synaptic transduction and plasticity.

Abbreviations

PNN, perineuronal nets; CNS, central nervous system; CSPG, chondroitin sulfate proteoglycans; AMPA receptor, α-amino-3-hydroxy-5-methyl-4-isoxazolepropionic acid receptor; WFA, *Wisteria floribunda* agglutinin; GalNAc, N-acetyl-galactosamine; CS, chondroitin sulfate; PSD95, postsynaptic density protein 95; ECM, extracellular matrix; 2D – two-dimensional; 3D – 3-dimensional; RMSD – root mean square deviation; BDNF, brain-derived neurotrophic factor; NT-3, neurotrophin-3; FGF, fibroblast growth factors; VEGF, vascular endothelial growth factor; GDNF, glial cell-derived neurotrophic factor; PTPsigma, receptor-type tyrosine-protein phosphatase S; Sema3A, Semaphorin-3A.

Key words: perineuronal nets, extracellular matrix, chondroitinsulfate proteoglycans, somatosensory cortex, synaptic plasticity, cell surface compartments

Introduction

Perineuronal nets (PNN) are formed on neuronal surface during early postnatal development as an important functional element of mature synaptic circuits (Medini and Pizzorusso, 2008; Dityatev et al., 2010; Kwok et al., 2012; Fawcett, 2015; Miyata et al., 2015). PNN are expressed in the brain cortex, hippocampus, cerebellum, spinal cord and other parts of the CNS. The role of PNN in maturation of the synaptic circuitry of parvalbumin-positive interneurons in somatosensory and visual cortex has been studied in particular detail (Pizzorusso et al., 2002; McRae et al., 2007; Miyata et al., 2012). PNN ensheath synaptic boutons on neuronal soma and proximal dendrites (Brückner et al., 2006; Carulli et al., 2013; Geissler et al., 2013). PNN consist of chondroitin sulfate proteoglycans (CSPG) assembled on the hyaluronan scaffold (Kwok et al., 2012). The PNN molecular complex involves tenascin R, link proteins and other CSPG binding molecules such as Sema3A and Otx2 (Carulli et al., 2006; Beurdeley et al., 2012; Carulli et al., 2013). PNN development is controlled by synaptic activity (Lander et al., 1998; Brückner et al., 2004; McRae et al., 2007; Carulli et al., 2010) and the formation of PNN terminates the critical period of synaptic plasticity (Pizzorusso et al., 2002; Miyata et al., 2015). Enzymatic digestion of PNN with chondroitinase ABC results in the relief of synaptic plasticity in adult animals (Pizzorusso et al., 2002). Genetic ablation of PNN components leads to retained synaptic plasticity in the adulthood (Carulli et al., 2010) and to abnormal synaptic transduction (Weber et al., 1999; Saghatelyan et al., 2001). It has been suggested that PNN may serve as a molecular substrate for the storage of long-lasting memories (Tsien, 2013).

At the level of molecular mechanisms it was shown that PNN constrains lateral mobility of extrasynaptic AMPA receptors in the plasma membrane and the exchange rate between the synaptic and extrasynaptic receptor pools (Frischknecht et al., 2009). Accordingly, the diffusion rates of AMPA receptors in cultured hippocampal neurons are reduced between the 2nd and 3rd weeks in culture – at the time when the PNN-like structure is formed on the neuronal surface (Borgdorff and Choquet 2002; John et al., 2006). ECM digestion with hyaluronidase reverses receptor mobility to the juvenile state and abrogates the pair-pulse depression of synaptic transduction (Frischknecht et al., 2009). This spatial constrain of the receptor mobility suggests that the PNN mesh geometry may serve as a potential regulatory factor that controls synaptic transduction. Furthermore the PNN mesh geometry may affect synaptic function and neuronal signaling by defining the cell surface distribution of neurotrophic factors and cation binding sites (Celio et al., 1998; Dityatev et al., 2010)

Wisteria floribunda agglutinin (WFA) is generally used as a PNN marker and ablation of a major CSPG aggrecan via siRNA or knock-out abrogates WFA staining of PNN (Kwok et al., 2010; Giamanco et al., 2010). WFA is believed to bind N-acetyl-galactosamine (GalNAc) of CS chains (Härtig et al., 1992). WFA staining is also sensitive to some extent to the sulfation pattern of GalNAc and mature PNN with high degree of 4-*O*-sulfation exhibit higher WFA reactivity (Miyata et al., 2012). Expression of the WFA-positive PNN is tightly connected to activation state of synaptic networks (McRae, 2007). Moreover at the microstructural and ultrastructural level WFA staining was used in combination with electron and fluorescent microscopy to visualize synapse ensheathment in PNN (Bruckner et al., 2006). Despite a number of pioneering works (reviewed in Celio et al., 1998; Bruckner et al., 2006;), the PNN microstructure received less attention so far as

compared to detailed investigation of molecular composition and functional role of the brain PNN (Miyata et al., 2012).

Here we obtained high resolution confocal images of PNN on the adult mouse and rat neurons from layers IV and VI of somatosensory cortex to analyze mesh geometry and fluorescence intensity distribution within individual meshes. We demonstrate spatial patterns of CSPG distribution at the single mesh level and organization of the cell surface PNN into clusters of meshes with specific morphology variants.

Results

PNN in somatosensory cortex

To study the PNN geometry we analyzed confocal images of the WFA-stained histological sections from adult rat and mouse somatosensory cortex (Figs.1A-E). We traced each mesh as a polygon (Figs.1F-G) and quantified the area, perimeter and the number of vertices. We performed this analysis on cell somata of 34 neurons from mouse cortex (total of 1274 meshes, 3 mice) and 36 neurons from rat cortex (total of 1139 meshes, 3 rats).

Mesh shape

A range of polygonal mesh shapes was observed in the cortex PNN with the number of vertices varying from 3 to 9. Vast majority of meshes have quadrangle, pentagon or hexagon shapes (Figs. 2A-F). Pentagon was the most frequently observed mesh shape that takes place in 44% of the mesh pool in mouse PNN and in 40% in rat PNN (Figs. 2A, B, C). Quadrangle, pentagon and hexagon shapes together represent 93% of meshes in mouse neurons and 87% in rat neurons (Fig. 2C).

Mesh area and perimeter

The mesh area varied widely within individual neurons (Fig. 2E). The mean mesh size was 1.29 (+/-0.67) μm^2 for mouse neurons and 1.44 (+/-0.26) μm^2 for rat neurons. Extreme area values varied widely with minimum value of 0.24 μm^2 and maximum value of 5.48 μm^2 for mouse neurons. The corresponding values for rat PNN were 0.29 μm^2 and 10.18 μm^2. The histogram of the mesh area demonstrates similar distribution for mouse and rat PNN (Fig. 2F). The area of the mesh projection in confocal plane may differ profoundly from the real mesh contour area depending on the mesh 3D orientation. To verify high variability of the mesh size observed in 2D analysis (Figs. 2E, F) we selected 20 smallest and 20 largest meshes from each mouse (Fig. 2I) and made 3D reconstruction for those meshes from confocal stacks, 9 planes (z dimension 1.8 μm) for each mesh with the Imaris Filament Autodepth tool (Figs. 2G, H). As quantification of the mesh area is complicated in 3D, we measured perimeter of the mesh 3D contour (total filament length for single mesh) and compared it to the 2D perimeter of the same meshes (Figs. 2J, K). As expected, variation of the mesh perimeter was less as compared to the variation of the mesh area (Figs. 2I, J), depicting the difference between the linear and square dimension. The 3D mesh perimeter and the 2D projection perimeter of the same meshes exhibited similar variation (Figs. 2J, K), indicating that the mesh size variation observed in the 2D analysis remains valid for the 3D analysis.

WFA intensity distribution within a single mesh

Individual meshes exhibit distinct patterns of the WFA intensity distribution along the mesh perimeter (Fig. 3). One variant is characterized by the WFA signal enrichment at vertices and lower intensity at the middles of the edges (Figs. 3A-D). We designate this type of meshes as polar meshes. The other type has relatively uniform distribution of the WFA staining intensity along the

mesh perimeter (Figs. 3E-F, H). We designate this second type of meshes as nonpolar. To quantify the WFA signal enrichment at the mesh vertices we took the ratio of mean intensity in the vertices (the vertex pixel plus one adjacent pixel on each side of the vertex) by the mean intensity of edge middle parts defined by 3-4 pixels in the middle of each edge. We designate this ratio as polarity index. The values of the polarity index vary from 0.8 to 4.66 in mouse PNN and from 0.97 to 4.42 in rat PNN. The mean values are 1.42 for mouse PNN and 1.43 for rat PNN and the histograms show similar distribution of the parameter for mouse and rat neurons (Fig. 3G). The intensity distribution within a mesh projection in confocal plane may differ profoundly from the real intensity distribution along the mesh contour depending on the mesh 3D orientation. To study the 3D profile of the WFA-positive epitope distribution we performed 3D reconstruction for 60 meshes selected randomly from 3 mice (20 meshes from each mouse) (Figs. 3I-L, Fig. S2). A stack of 9 confocal planes was used for each mesh. Intensity values were quantified with the Imaris Meausurement Points tool (Figs. 3I, J). High correlation was observed for the 2D and 3D polarity index values, correlation coefficient r=0.83 (Fig. 3K).

Cell surface clusters of meshes with distinct morphology variants

To reveal spatial distribution of the two patterns (Fig. 3) we set an arbitrary threshold value of 1.5 for the polarity index and mapped the polar and nonpolar meshes on the PNN confocal images (Figs. 4A-B). We observed that meshes of the same spatial pattern often form clusters and thereby segregate from meshes of the other pattern (Figs. 4A-B). We then asked whether such clusters are observed sporadically at certain threshold values or whether a gradual change in mesh polarity could be traced at sequential threshold steps. We observed gradual change of continuing cluster borders when changing the polarity threshold for some of the clusters (Fig. 4E). We then performed 3D analysis on the same images where clusters were revealed by the 2D analysis. For each mouse 3 polar and 3 nonpolar clusters were analyzed (total number 71 polar and 58 nonpolar meshes, total number of clusters 18, n=3) in the same way as in (Figs. 3I, L, Fig. S2). A confocal stack of 9 planes was analyzed for each mesh (4 planes above and 4 planes below the best focus plane). We observed 15 out of 18 clusters preserved in 3D reconstructions of confocal stacks (Figs. 3, 4). Quantification of the coincidence of cell surface PNN clusters obtained by 2D and 3D analysis demonstrates 82% match for meshes in polar clusters and 77% match for nonpolar clusters (Figs. 4A-D, F).

Co-localization of vertices with local CSPG density maxima in polar and nonpolar meshes

To have a post hoc unbiased estimation of the PNN polarity patterns proposed here in relation to the brain WFA-positive CSPG ECM distribution we used the “Find maxima” tool of the Fiji software. This procedure automatically detects local intensity maxima in microscopy images. Some mesh vertices exhibit close match with the automatically detected intensity maxima (Fig. 5A) in single confocal sections while others show no obvious co-localization (Fig. 5B). We selected meshes with low (0.8-1.1) or high (2-4.7) values of the polarity index, each group representing about 8% of the whole pool of mouse PNN analyzed in the present study. Root mean square deviation (RMSD) was calculated between vertex coordinates and local intensity maxima coordinates that fell within 0.5 μm distance from each vertex. The RMSD values were lower for polar meshes as compared to nonpolar meshes (Fig. 5C). This result demonstrates that the two spatial patterns of PNN morphology can be distinguished based on the quantitative criterion that is not influenced by manual tracing and represents total distribution of the WFA-positive CSPG epitopes in the ECM of mouse brain cortex.

Discussion

Extensive studies over the last two decades demonstrate that PNN formation is controlled by synaptic activity (Brückner et al., 2004; McRae et al., 2007; reviewed in Miyata and Kitagawa, 2015). After the PNN is assembled it in turn starts to control synaptic transmission (Pizzorusso et al., 2002, Medini and Pizzorusso, 2008).. This tight bidirectional connection between PNN and synaptic transduction (Miyata and Kitagawa, 2015) suggests the existence of structural and functional mechanisms connecting synapses to the surrounding PNN molecular complexes.

Quantitative information on the PNN architecture is particularly interesting from the point of structural relation between PNN and synapses on the neuronal cell surface. Transmission electron microscopy data demonstrate that PNN delineate the physical borders of presynaptic terminals and demarcate the border between neighboring synapses (Bruckner et al., 2006). These data are further supported by confocal microscopy with a presynaptic marker of GABA-ergic synapses (Bruckner et al., 2006), a presynaptic marker of glutamatergic synapses (Miyata et al., 2012), a more general presynaptic marker Bassoon and postsynaptic marker PSD95 (Geissler et al., 2013).

The heterogeneity of the mesh size demonstrated in the present study (Figs. 2D-I) imposes a few questions. First, to what extent does the mesh size reflect the size of the individual synapse and what functional consequences are determined by the size of this ECM-synapse structure? And second, how dynamic is the mesh structure in the brain tissue, do meshes change their size adopting to the synaptic network state or do they keep their size constant? What is the functional meaning of the extreme values of the mesh size? Do the smallest meshes represent functional synapses? Are they “newborn meshes” that are going to extend to a larger size? Or did they shrink from a medium size for a functional adjustment or because the corresponding synapses were eliminated? Do meshes shrink and expand to adapt to the local or global changes of the cell body curvature?

PNN restrict lateral mobility of neurotransmitter receptors on the neuronal cell surface and the exchange rate between synaptic and extrasynaptic receptor pools (Frischknecht et al., 2009). These data suggest that PNN might have a role in dividing the cell surface into compartments and creating boundaries for the 2-dimentional diffusion of molecules with large extracellular domains between neighboring meshes. The size of individual compartments, i.e. meshes, may potentially affect the receptor kinetics in the plasma membrane. Indeed, the constrains of the receptor lateral diffusion promote receptor oligomerization and act as a regulator of receptor activation (Grecco and Bastiaens, 2011). Thus the mesh size variation demonstrated in the present study (Fig. 2) suggests one possible mechanism for the regulation of synaptic function through morphological constrains of the mesh size. It is important to note that the effect of ECM on receptor mobility varies between neuronal types and other factors may overrule the function of PNN. In the aspiny glutamatergic synapses of cultured hippocampal interneurons the AMPA receptor motility is strongly affected by chelation of intracellular calcium and not by the ECM digestion (Klueva et al., 2014).

Current knowledge on the CSPG signaling and protein complex formation at the neuronal cell surface suggests that the spatial distribution of CSPG in the PNN may control synaptic function via a number of mechanisms (Kwok et al., 2011; Miyata et al., 2012; Fawcett, 2015). Experimental evidence suggests that the CSPG ECM set up the spatial framework for the ordered distribution of the proteoglycan-binding ligands Sema3A, Otx2 and tenascins across the synaptic field on the neuronal cell surface (Beurdeley et al., 2012; Carulli et al., 2013; Dick et al., 2013). Neurotrophic factors BDNF, NT-3, FGF, VEGF, pleiotrophin and GDNF family ligands bind with high affinity to glycosaminoglycans (Milev et al., 1998; Nandini et al., 2004; Kanato et al., 2009) so that their

distribution on neuronal surface may be also controlled by the PNN structure. This spatial order may dictate the ligand enrichment at the hubs connecting 3-4 neighbouring synapses in some cells (Figs. 3A-D, Fig. 4, Fig. S2) or, alternatively, set up uniform distribution along the mesh borders (Figs. 3E, F, H, Fig. 4, Fig. S2). This spatial distribution of the CSPG-bound ligands may contribute to regulation of the crosstalk between neighboring synapses. Furthermore, the results of the present study suggest that the distribution of CSPG and their binding partners on the PNN meshwork may be spatially organized into distinct areas (clusters) on the surface of a single neuronal cell (Fig. 4, Fig. S2).

A mechanism defining polarized versus uniform pattern of a particular mesh is probably related to the PNN molecular composition at a specific portion of the neuronal cell surface. The results of the present study suggest that PNN are condensed to various extent along the mesh perimeter so that the CS chain density is highest at the mesh vertices in polarized meshes. By contrast, the CS density is likely to be distributed irregularly in the meshes with nonpolar pattern. In the present study we revealed mesh clusters on neuronal surface as a result of the examination of the PNN microstructure. Understanding the functional meaning of those clusters would be of particular interest. Literature data on PNN suggest that those areas may represent groups of neighboring synapses on the neuronal cell surface (Brückner et al., 2006; Miyata et al., 2012; Carulli et al., 2013; Geissler et al., 2013). The question arises whether the PNN morphology-based clusters are functionally connected to the regulation of synaptic transmission. An interesting possibility is that meshes could be grouped into clusters based on modality of the synaptic input information. This spatial segregation of the PNN pattern may provide an additional mechanism for functional compartmentation of neuronal cells.

Here we used both 2D and 3D confocal image analysis to quantify intensity distribution at a single mesh level. First we used the 2D polarity index defined as the ratio of mean intensity in vertices to the mean intensity of edge middle parts. The advantage of the 2D analysis in this particular case was the ability to collect quantitative parameters for over 2400 meshes in 70 neurons. This allowed us to reveal the clusters on neuronal cell surface by using a range of threshold values for the polarity index (Fig. 4 A, B, E). From the technical point of logistics it was most crucial that Fiji was an open source software allowing for sufficient scale of data analysis. The critical limitation of the 2D analysis is the loss of spatial information about the 3D shape and CS density distribution in the PNN (Figs. 2, 3).

The 3D analysis was performed to ensure more accurate quantification of the mesh geometry and intensity distribution within the PNN volume. The 3D analysis allowed a better estimation of the mesh perimeter and confirmed the heterogeneity of the mesh size in the analyzed PNN (Figs. 2G-K). The 3D analysis demonstrated high correlation between the 2D and 3D polarity indices (Figs. 3I-L) and confirmed the presence of the clusters of meshes with distinct morphologies on neuronal surface (Fig. 4 and Fig. S2). The crucial limitation of the 3D analysis is the difficulty to calculate automatically a range of parameters for the PNN geometry (including the mesh area) in 3D space resulting in highly time-consuming procedures for manual measurements and data collection. An outlook on limitations, future developments and potential solutions for the PNN microstructure analysis is given in Table 1.

In summary, our results demonstrate that the PNN spatial framework is organized in distinct patterns at the microstructural level. This may provide an additional mechanism for compartmentation of neuronal surface and regulation of multiple signaling processes, including synaptic plasticity.

Table 1. Limitations of the PNN structural analysis and potential solutions.

Limitations	Future developments and potential solutions
In the present study the level of detail is narrowed by the confocal microscopy resolution limit. The method is fine to distinguish the CS epitope enrichment in the mesh nodes versus middle parts of the edges.	Superresolution light microscopy or electron microscopy would give advanced detalization on the PNN structure.
The critical limitation of the 2D analysis is the loss of spatial information about the 3D shape and CS density distribution in the PNN. 2D analysis is sufficiently fast to analyze thousands of meshes in reasonable time.	A tool could be developed to detect PNN regions that are parallel to the focal plane. Those regions could be analyzed more adequately with 2D tools.
The main limitation of the 3D analysis is the difficulty to calculate automatically a range of parameters for the PNN geometry (including intensity values from different parts of a mesh) in 3D space resulting in highly time-consuming procedures for manual measurements and data collection.	Additional procedures could be possibly developed for automated 3D analysis. Those may include the mesh area calculation and automated mesh border tracing.
As the neurite curvature is different as compared to the cell soma we can not claim that the 2D-3D match of the CSPG intensity distribution is valid for neurites.	A tool could be developed to detect neurite PNN meshes that are parallel to the focal plane. Those meshes could be analyzed more adequately with 2D tools.

Methods

Tissue preparation

Adult mouse and rat brain samples were collected according to regulations of the ethics committee of Kazan Federal University. For immunohistochemistry animals were terminally anaesthetized with an intraperitoneal overdose of Urethane (Sigma-Aldrich) and were immediately perfused through the heart with 150 ml of cold phosphate- buffered saline (PBS, pH 7.4), followed by 150 ml cold 4% paraformaldehyde. Brains were removed and postfixed overnight in 4% paraformaldehyde. After that brains were cryoprotected with 30% sucrose for 48 h and then frozen in embedding medium. All samples were stored at – 80°C until sectioning. Thirty-micrometer-thick coronal brain sections were cut on a cryostat. The primary somatosensory cortex regions were determined using Comparative Cytoarchitectonic Atlas of Mouse Brain (Patrick R. Hof, Elsevier) and The Rat Brain in Stereotaxic Coordinates (George Paxinos & Charles Watson, Fourth Edition, 1998).

WFA staining

For staining of PNNs we used biotinylated *Wisteria floribunda* Lectin (VectorLab, USA). The staining was performed on free-floating sections. All incubations were carried out in 24-well plates with 500 µl per well. After sectioning samples were washed three times using phosphate- buffered saline (PBS; pH 7.4) to remove embedding medium . Free-floating sections were treated for 1 h with a blocking solution - 3% normal goat serum (NGS) (JacksonImmuno Research, USA) in 0.1M PBS with 0.5% Triton X-100 (PBST). Streptavidin/Biotin Blocking Kit (VectorLab, USA) was used

according to the manufacturers protocol to block endogenous biotin. After that sections were quickly rinsed in PBS and incubated overnight at +4°C using biotinylated *Wisteria floribunda* agglutinin with final concentration 2µg/ml (dilution 1:1000) in 10 mM HEPES and 0.15 M sodium chloride, pH 7.4.

Samples were washed three times for 15 minutes with PBS and incubated for 30 min with AlexaFluor633-conjugated streptavidin (Invitrogen) (dilution 1:500). Finally, the sections were washed with PBS during 10 minutes and placed in phosphate buffer (PB, pH7.4). The sections were mounted on slides, air-dried and coverslipped with ImmunoMount (ThermoScientific).

Epifluorescent microscopy

Epifluorescent images were taken with Zeiss Axio Imager 2.0 microscope and Zeiss AxioCam HRc digital camera (Carl Zeiss Microscopy). FIJI software was used to montage and process the images with minimal alterations to the contrast and background.

Confocal microscopy

The sections were imaged with laser confocal microscope LSM780 (Carl Zeiss, Jena, Germany), objective lenses were Plan-Apochromat 5x/0.16 M27 and Plan-Apochromat 63x/1.40 Oil DIC M27. Voxel size of 100x100x200 nm was used for high resolution imaging.

Image analysis

Quantitative image anlysis of single confocal planes was performed with FIJI (Schindelin et al., 2012). Meshes were traced on neuronal cell bodies. The mesh area was calculated with FIJI as follows: the mesh vertices were defined with the Point Picker tool in Fiji (Fig.1F). All pixels belonging to a particular mesh were selected via the makeSelection Fiji command as a polygon based on the vertex coordinates. All pixels of the polygon were quantified via the getHistogram Fiji command. The mesh area was calculated as the sum of pixel counts for the whole range of intensity values.

Polarity index was calculated as the ratio of mean intensity in vertices defined by 3 pixels in each vertex to the mean intensity of edge middle parts defined by 3-4 pixels in the middle of each edge.

Three-dimensional reconstruction of confocal data was performed with Imaris sotware (Bitplane).

We used the Imaris filament tool ("dendrite" variant) with the Autodepth option for manual tracing. A z-stack of 9 confocal planes was analyzed for each mesh (4 planes above and 4 planes below the best focus plane) so that the z dimension of the analyzed volume was 1.8 µm. Filaments were traced along the mesh border and z-position of each filament point was selected automatically based on the intensity distribution. The 3D mesh perimeter was quantified as the total length of the filament tracing the mesh.

For the polarity index quantification intensity values were collected for vertices and for filament points in the middle of each edge with the Imaris Measurement Points tool. The 3D polarity index was calculated for each mesh as the mean vertex intensity divided by the mean intensity of the middle points of the mesh edges.

To compare the mesh polarity quantification by Fiji 2D and Imaris 3D procedures meshes were selected with random integer generator (www.random.org).

Coincidence of cell surface PNN clusters obtained by 2D and 3D analysis was calculated as percent of meshes that fell into the same cluster based on the 2D and 3D analyses. 3D reconstruction was performed on 3 polar and 3 nonpolar clusters previously detected with 2D analysis (cluster size 4-12 meshes) from each mouse. Total number - 9 polar and 9 nonpolar clusters (n=3).

In all experiments statistical significance was calculated for the data from 3 independent experiments using one-way ANOVA (Excel, Microsoft). Error bars represent standard error of mean (SEM), symbols *, ** and *** represent $P<0.05$, 0.01 and 0.001, respectively.

Acknowledgements

We are thankful to Harri Jantola, Kimmo Tanhuanpää and Mika Molin for their generous help with image analysis. Anastasia Kochneva is acknowledged for assistance with mesh tracing. The work was supported by the Academy of Finland grant 1268543 and by Neuroscience Center, University of Helsinki. Sample preparation was supported by the Russian Science Foundation grant 14-15-00916. The work was performed according to the Russian Government Program of Competitive Growth of Kazan Federal University.

References

Beurdeley, M., Spatazza, J., Lee, H.H.C., Sugiyama, S., Bernard, C., Di Nardo, A. A., Hensch, T.K., Prochiantz, A., 2012. Otx2 binding to perineuronal nets persistently regulates plasticity in the mature visual cortex. J. Neurosci. 32, 9429–9437. doi:10.1523/JNEUROSCI.0394-12.2012

Borgdorff, A.J., Choquet, D., 2002. Regulation of AMPA receptor lateral movements. Nature 417, 649–653. doi:10.1038/nature00780

Brückner, G., Kacza, J., Grosche, J., 2004. Perineuronal nets characterized by vital labelling, confocal and electron microscopy in organotypic slice cultures of rat parietal cortex and hippocampus. J. Mol. Histol. 35, 115–122. doi:10.1023/B:HIJO.0000023374.22298.50

Brückner, G., Szeöke, S., Pavlica, S., Grosche, J., Kacza, J., 2006. Axon initial segment ensheathed by extracellular matrix in perineuronal nets. Neuroscience 138, 365–375. doi:10.1016/j.neuroscience.2005.11.068

Carulli, D., Foscarin, S., Faralli, A., Pajaj, E., Rossi, F., 2013. Modulation of semaphorin3A in perineuronal nets during structural plasticity in the adult cerebellum. Mol. Cell. Neurosci. 57, 10–22. doi:10.1016/j.mcn.2013.08.003

Carulli, D., Pizzorusso, T., Kwok, J.C.F., Putignano, E., Poli, A., Forostyak, S., Andrews, M.R., Deepa, S.S., Glant, T.T., Fawcett, J.W., 2010. Animals lacking link protein have attenuated perineuronal nets and persistent plasticity. Brain 133, 2331–2347. doi:10.1093/brain/awq145

Carulli, D., Rhodes, K.E., Brown, D.J., Bonnert, T.P., Pollack, S.J., Oliver, K., Strata, P., Fawcett, J.W., 2006. Composition of perineuronal nets in the adult rat cerebellum and the cellular origin of their components. J. Comp. Neurol. 494, 559–577. doi:10.1002/cne.20822

Celio, M.R., Spreafico, R., De Biasi, S., Vitellaro-Zuccarello, L., 1998. Perineuronal nets: past and present. Trends Neurosci. 21, 510-515.

Dick, G., Liktan, C., Alves, J.N., Ehlert, E.M.E., Miller, G.M., Hsieh-Wilson, L.C., Sugahara, K., Oosterhof, A., Van Kuppevelt, T.H., Verhaagen, J., Fawcett, J.W., Kwok, J.C.F., 2013. Semaphorin 3A binds to the perineuronal nets via chondroitin sulfate type E motifs in rodent brains. J. Biol. Chem. 288, 27384–27395. doi:10.1074/jbc.M111.310029

Dityatev, A., Seidenbecher, C.I., Schachner, M., 2010. Compartmentalization from the outside: The extracellular matrix and functional microdomains in the brain. Trends Neurosci. 33, 503-512. doi:10.1016/j.tins.2010.08.003

Fawcett, J.W., 2015. The extracellular matrix in plasticity and regeneration after CNS injury and neurodegenerative disease. Prog. Brain Res. 218, 213–226. doi:10.1016/bs.pbr.2015.02.001

Frischknecht, R., Heine, M., Perrais, D., Seidenbecher, C.I., Choquet, D., Gundelfinger, E.D., 2009. Brain extracellular matrix affects AMPA receptor lateral mobility and short-term synaptic plasticity. Nat. Neurosci. 12, 897-904. doi:10.1038/nn.2338

Geissler, M., Gottschling, C., Aguado, A., Rauch, U., Wetzel, C.H., Hatt, H., Faissner, A., 2013. Primary hippocampal neurons, which lack four crucial extracellular matrix molecules, display abnormalities of synaptic structure and function and severe deficits in perineuronal net formation. J. Neurosci. 33, 7742–7755. doi:10.1523/JNEUROSCI.3275-12.2013

Giamanco, K. A., Morawski, M., Matthews, R.T., 2010. Perineuronal net formation and structure in aggrecan knockout mice. Neuroscience 170, 1314–1327. doi:10.1016/j.neuroscience.2010.08.032

Härtig, W., Brauer, K., Brückner, G., 1992. *Wisteria floribunda* agglutinin-labelled nets surround parvalbumin-containing neurons. Neuroreport 3, 869–872. doi:10.1097/00001756-199210000-00012

John, N., Krügel, H., Frischknecht, R., Smalla, K.-H., Schultz, C., Kreutz, M.R., Gundelfinger, E.D., Seidenbecher, C.I., 2006. Brevican-containing perineuronal nets of extracellular matrix in dissociated hippocampal primary cultures. Mol. Cell. Neurosci. 31, 774–784. doi:10.1016/j.mcn.2006.01.011

Kanato, Y., Ono, S., Kitajima, K., Sato, C., 2009. Complex formation of a brain-derived neurotrophic factor and glycosaminoglycans. Biosci. Biotechnol. Biochem. 73, 2735-2741.

Klueva, J., Gundelfinger, E.D., Frischknecht, R.R., Heine, M., 2014. Intracellular Ca^{2+} and not the extracellular matrix determines surface dynamics of AMPA-type glutamate receptors on aspiny neurons. Philos. Trans. R Soc Lond B Biol Sci. 369, 20130605. doi: 10.1098/rstb.2013.0605.

Kwok, J.C.F., Carulli, D., Fawcett, J.W., 2010. In vitro modeling of perineuronal nets: Hyaluronan synthase and link protein are necessary for their formation and integrity. J. Neurochem. 114, 1447–1459. doi:10.1111/j.1471-4159.2010.06878.x

Kwok, J.C.F., Dick, G., Wang, D., Fawcett, J.W., 2011. Extracellular matrix and perineuronal nets in CNS repair. Dev. Neurobiol. 71, 1073–1089. doi:10.1002/dneu.20974

Kwok, J.C.F., Warren, P., Fawcett, J.W., 2012. Chondroitin sulfate: A key molecule in the brain matrix. Int. J. Biochem. Cell Biol. 44, 582–586. doi:10.1016/j.biocel.2012.01.004

Lander, C., Zhang, H., Hockfield, S., 1998. Neurons produce a neuronal cell surface-associated chondroitin sulfate proteoglycan. J. Neurosci. 18, 174–183.

McRae, P.A., Rocco, M.M., Kelly, G., Brumberg, J.C., Matthews, R.T., 2007. Sensory deprivation alters aggrecan and perineuronal net expression in the mouse barrel cortex. J. Neurosci. 27, 5405-5413.

Medini, P., Pizzorusso, T., 2008. Visual experience and plasticity of the visual cortex: a role for epigenetic mechanisms. Front. Biosci. 13, 3000–3007. doi:10.1016/j.conb.2009.05.009

Milev, P., Chiba, A., Häring, M., Rauvala, H., Schachner, M., Ranscht, B., Margolis, R.K.,

Margolist, R.U., 1998. High affinity binding and overlapping localization of neurocan and phosphacan/protein-tyrosine phosphatase-ζ/β with tenascin-R, amphoterin, and the heparin-binding gowth-associated molecule. J. Biol. Chem. 273, 6998–7005. doi:10.1074/jbc.273.12.6998

Miyata, S., Kitagawa, H., 2015. Mechanisms for modulation of neural plasticity and axon regeneration by chondroitin sulphate. J. Biochem. 157, 13–22. doi:10.1093/jb/mvu067

Miyata, S., Komatsu, Y., Yoshimura, Y., Taya, C., Kitagawa, H., 2012. Persistent cortical plasticity by upregulation of chondroitin 6-sulfation. Nat. Neurosci. 15, 414–422. doi:10.1038/nn.3023

Nandini, C.D., Mikami, T., Ohta, M., Itoh, N., Akiyama-Nambu, F., Sugahara, K., 2004. Structural and functional characterization of oversulfated chondroitin sulfate/dermatan sulfate hybrid chains from the notochord of hagfish. Neuritogenic and binding activities for growth factors and neurotrophic factors. J. Biol. Chem. 279, 50799–50809. doi:10.1074/jbc.M404746200

Pizzorusso, T., Medini, P., Berardi, N., Chierzi, S., Fawcett, J.W., Maffei, L., 2002. Reactivation of ocular dominance plasticity in the adult visual cortex. Science. 298, 1248–1251. doi:10.1126/science.1072699

Saghatelyan, A.K., Dityatev, A., Schmidt, S., Schuster, T., Bartsch, U., Schachner, M., 2001. Reduced perisomatic inhibition, increased excitatory transmission, and impaired long-term potentiation in mice deficient for the extracellular matrix glycoprotein tenascin-R. Mol. Cell. Neurosci. 17, 226–240. doi:10.1006/mcne.2000.0922

Schindelin, J., Arganda-Carreras, I., Frise, E., Kaynig, V., Longair, M., Pietzsch, T., Preibisch, S., Rueden, C., Saalfeld, S., Schmid, B., Tinevez, J.Y., White, D.J., Hartenstein, V., Eliceiri, K., Tomancak, P., Cardona, A., 2012. Fiji: an open-source platform for biological-image analysis. Nat. Methods. 9, 676-682. doi: 10.1038/nmeth.2019.

Tsien, R.Y., 2013. Very long-term memories may be stored in the pattern of holes in the perineuronal net. Proc. Natl. Acad. Sci. 110, 12456–12461. doi:10.1073/pnas.1310158110

Vo, T., Carulli, D., Ehlert, E.M.E., Kwok, J.C.F., Dick, G., Mecollari, V., Moloney, E.B., Neufeld, G., de Winter, F., Fawcett, J.W., Verhaagen, J., 2013. The chemorepulsive axon guidance protein semaphorin3A is a constituent of perineuronal nets in the adult rodent brain. Mol. Cell. Neurosci. 56, 186–200. doi:10.1016/j.mcn.2013.04.009

Weber, P., Bartsch, U., Rasband, M.N., Czaniera, R., Lang, Y., Bluethmann, H., Margolis, R.U., Levinson, S.R., Shrager, P., Montag, D., Schachner, M., 1999. Mice deficient for tenascin-R display alterations of the extracellular matrix and decreased axonal conduction velocities in the CNS. J. Neurosci. 19, 4245–4262.

Figure 1. PNN structure was analysed in adult mouse and rat cortical neurons. A. WFA-positive PNN in layers IV and VI of mouse somatosensory cortex. B. Render image of a confocal stack in cortical layer IV from the area marked in (A). Squares indicate areas shown in C-E. Cell bodies and proximal dendrites are covered with PNN. C-E. Meshwork structure of PNN on cell surface of neurons marked in (B). The enlarged subcellular areas are from single confocal planes. F. The mesh tracing procedure with Fiji software of the area marked in (E). For each mesh vertices were mapped manually on the original confocal image. G. The result of mesh tracing in (E). The mesh contours were mapped automatically based on the vertex coordinates. The scale bar in (A) is 100 μm, in (B) 10 μm, in (C-E) 2 μm, in (F) 1 μm . The scale bar in (F) is valid for (F-G).

Figure 2. Heterogeneity of mesh shape and size. A-B. Meshes have the shape of triangle, quadrilateral, pentagon, hexagon and polygons with higher number of vertices. C. Histogram of the mesh distribution with regard to the number of vertices in mouse and rat neurons, 1274 meshes measured from mouse neurons and 1139 meshes from rat neurons. D. Mesh size varies widely within individual neurons. A representative confocal image of a mouse neuron. E. PNN traced in two areas of the image in (D). Extreme values of the mesh area are shown in square micrometers. F. Histogram of the mesh area distribution in mouse and rat neurons, the same dataset as in (C). G, H. A large subpopulation of meshes have sloped orientation in relation to the focal plane as demonstrated by 3D Imaris reconstruction of the mesh perimeter with filament autodepth tracing. The XY (G) and XZ (H) orientations are shown for the same mesh. I. The 2D area difference between 60 smallest and 60 largest meshes selected for the 3D reconstruction from the 2D analysis results (20+20 meshes from each mouse). J. The 2D perimeter values for the same meshes as in (I). K. The 3D perimeter values for the same meshes as in (I). One way ANOVA was used in I, J, K, the number of independent experiments n=3.

Figure 3. Two distinct patterns of chondroitin sulfate distribution within a single mesh. A. Three meshes with node-enriched (polar) distribution of the WFA-binding epitope in a mouse neuron. B. The mesh perimeter traced. Vertices 1-4 are shown. C. Three dimentional reconstruction of WFA intensity distribution for the area shown in (A), (B). An isosurface for the fluorescence intensity threshold 20 a.u. is shown in green, semitransparent. An isosurface with intensity threshold 42 a.u. is shown in red. Areas of high intensity are shown for the vertices 1-4 of the mesh traced in (B). D. WFA intensity profile along the perimeter of the mesh traced in (B). Vertices are shown in purple. Vertice numbers are the same as in (B), (C). E. A mesh with uniform (non-polar) distribution of the WFA-binding epitope in a rat neuron. F. The mesh perimeter traced. Vertices 1-6 are shown.
G. Polarity index distribution in mouse and rat PNN. Calculated for the same dataset as in Fig. 2 C.
H. WFA intensity profile along the perimeter of the mesh traced in (F). Vertices are shown in purple. Vertice numbers are the same as in (F). I, J, L 3D Imaris reconstruction of the mesh perimeter with filament autodepth tracing. Vertices are shown in purple, middle pixels of each edge are shown in green. Intensity values of the mesh vertices and middle pixels of each edge are shown in (I). J. Vertices A, B, D, F are surrounded by small volumes of high density of the WFA-positive epitopes. An isosurface for the fluorescence intensity threshold 16 a.u. is shown in green, semitransparent. An isosurface with intensity threshold 65 a.u. is shown in red. K. Correlation for the 2D and 3D polarity index values, correlation coefficient r=0.83. L. The XZ orientation is shown for the same mesh as in (I, J). The scale bar in (A), (E) is 1 μm, in (B) – 0.5 μm, in (I), (J) – 5 μm. The scale bar

in (A) is valid for (A), (B), in (E) – for (E), (F).

Figure 4. Cell surface clusters with node-enriched and uniform distribution of WFA-binding epitopes. A. PNN traced on a mouse neuron cell body and meshes with polarity index above 1.5 marked with yellow dots. A cluster of nonpolar meshes (center, mesh number 10, 12, 13, 19-22, 31) is flanked by two clusters of polar meshes. B. A cluster of polar meshes and 3 clusters of nonpolar meshes in PNN on a mouse neuron. C, D. 3D reconstruction and polarity quantification in the same area as in A, B. Polar cells are shown in green, nonpolar – in blue. Polarity index threshold set to 1.5 in A-D. The same clusters were detected with 2D and 3D analysis with one exception: please note nonpolar cell 19 in B that becomes polar in D leading to disappearance of the nonpolar cluster. E. The polar cluster border was traced on a rat neuron at four sequential thresholds of polarity index (1.4, 1.5, 1.7, 1.8). The color code for the polarity threshold values is shown on the right. F. Quantification of coincidence of cell surface PNN clusters obtained by 2D and 3D analysis. 3D reconstruction was performed on 3 polar and 3 nonpolar clusters previously detected with 2D analysis (cluster size 4-12 meshes) from each mouse. Total number - 9 polar and 9 nonpolar clusters (n=3).

Figure 5. Co-localization of vertices with local CSPG density maxima in polar and nonpolar meshes. A. Local intensity maxima were determined with the Fiji find maxima tool in PNN confocal images. The automatically detected maxima are shown in blue, mesh vertices in yellow, coincidence in green. B. In many PNN areas the automatically detected maxima exhibit weak or no co-localization with mesh polygons. C. Root mean square deviation was calculated for vertices of nonpolar (polarity index 0.8-1.1) and highly polar (polarity index 2-4.7) meshes in relation to the automatically detected maxima within the radius of 5 pixels around each vertex. One way ANOVA was used in C, the number of independent experiments n=3.

Supplementary Figure 1. PNN structure was analysed in adult mouse and rat cortical neurons. A, F. WFA-positive PNN in layers IV and VI of mouse somatosensory cortex. B, G. Render images of confocal stacks in cortical layer IV from the areas marked in (A) and (F), respectively. Squares indicate areas shown in C-E, H, I. Cell bodies and proximal dendrites are covered with PNN. C-E. Meshwork structure of PNN on cell surface of neurons marked in (B). H-I. Meshwork structure of PNN on cell surface of neurons marked in (G). The enlarged subcellular areas are from single confocal planes in C-E, H, I.

Supplementary Figure 2. Polar and nonpolar meshes within the cell surface clusters. A. 3D reconstruction of PNN in the same neuron as in Fig. 4A, C. The meshes shown in (B-E) are marked in A. B-C. Node-enriched distribution of the WFA-positive epitopes in polar PNN meshes. Vertices are shown in purple, middle pixels of each edge are shown in green. Intensity values collected with the Measurement Points tool are shown for vertices and for the middle pixels of each edge. The mesh 3D polarity index is 1.9 in (B) and 2.3 in (C). D-E. Irregular distribution of the WFA-positive epitopes in nonpolar PNN meshes. The mesh 3D polarity index is 1.2 for (D) and (E). F-I. Isosurfaces for low fluorescence intensity thresholds are shown in green, semitransparent. The threshold values are 18, 28, 49, 30 for (F, G, H, I), respectively. Isosurfaces for high intensity thresholds are shown in red. The threshold values are 78, 78, 105, 119 for (F, G, H, I), respectively. Please note that the vertices are embedded in the local volumes with the highest intensity predominantly in (F, G) and to a less extent in (H, I). J, K, L. The XZ orientation is shown for the

same meshes as in (B, C, D) respectively. M. The XZ orientation is shown for the same mesh as in (E). An isosurface with intensity threshold 135 a.u. is shown in red.

Highlights

- Quantitative parameters of the perineuronal net geometry are reported for cortex.
- There are two pattern variants of chondroitin sulfate distribution for a single mesh.
- PNN is organized into clusters of meshes with distinct morphologies.

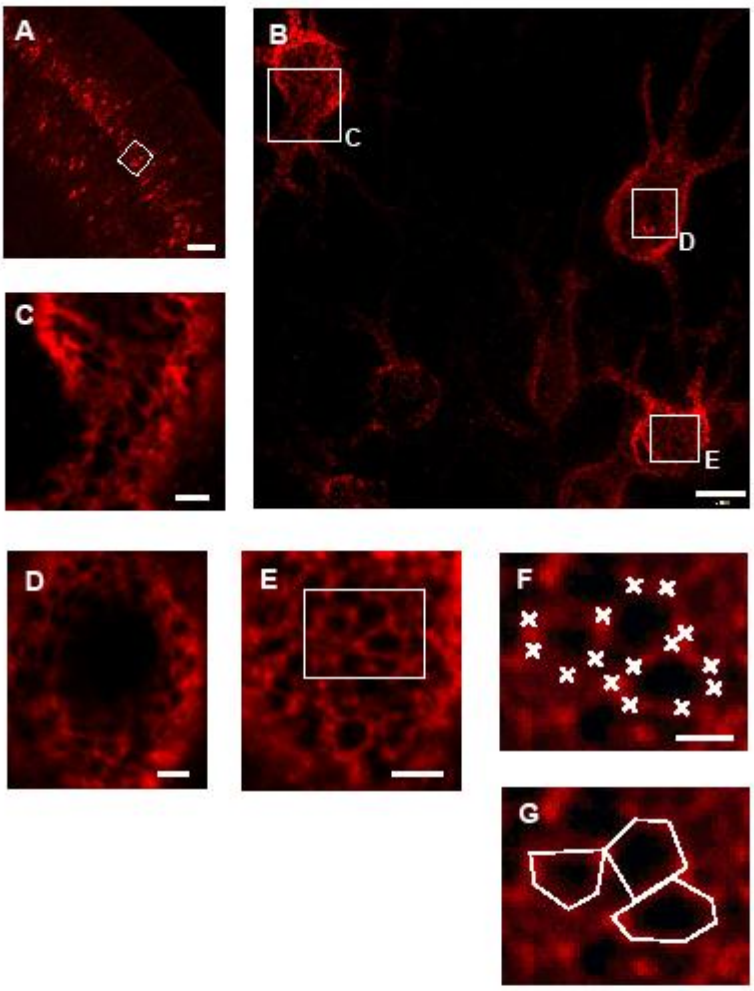

Arnst et al., Figure 1

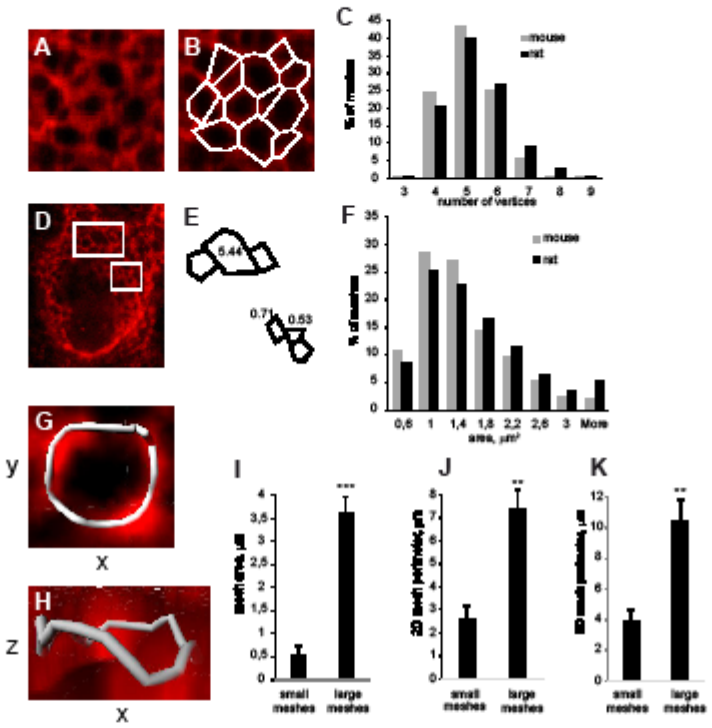

Arnst et al., Figure 2

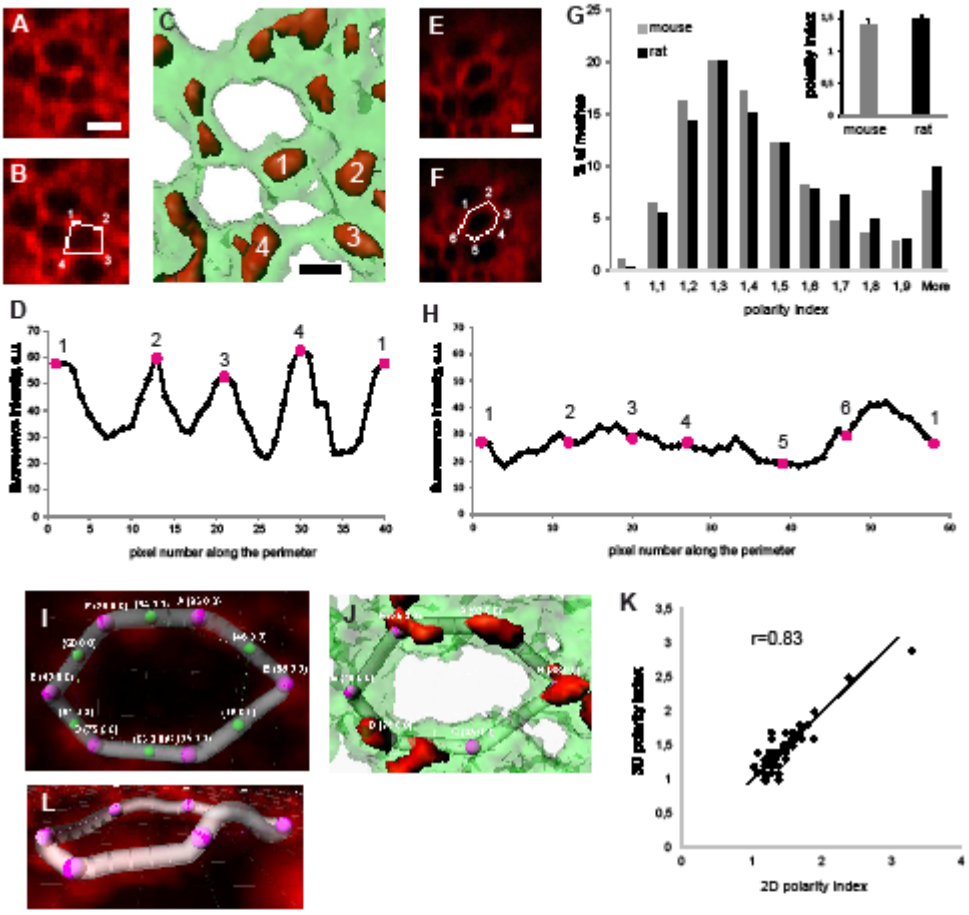

Arnst et al., Figure 3

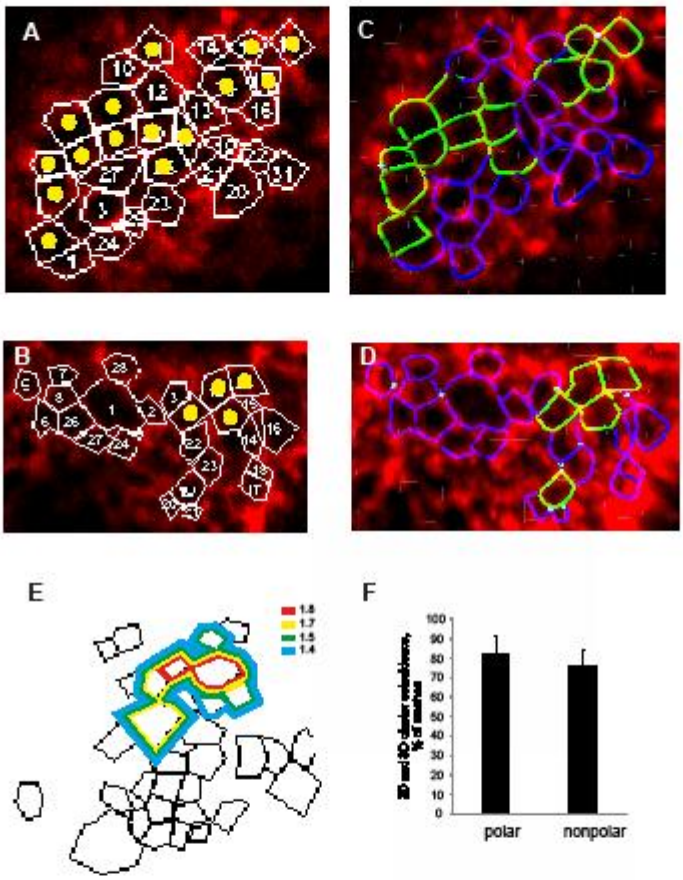

Arnst et al., Figure 4

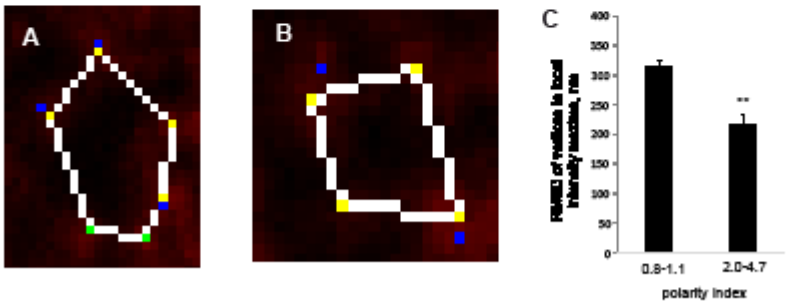

Arnst et al., Figure 5